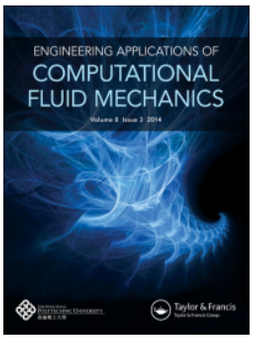

Taylor & Francis
Taylor & Francis Group

Engineering Applications of Computational Fluid Mechanics

ISSN: (Print) (Online) Journal homepage: https://www.tandfonline.com/loi/tcfm20

Numerical investigations of pipe flow downstream a flow conditioner with bundle of tubes

Guang Yin, Muk Chen Ong & Puyang Zhang

To cite this article: Guang Yin, Muk Chen Ong & Puyang Zhang (2023) Numerical investigations of pipe flow downstream a flow conditioner with bundle of tubes, Engineering Applications of Computational Fluid Mechanics, 17:1, e2154850, DOI: 10.1080/19942060.2022.2154850

To link to this article: https://doi.org/10.1080/19942060.2022.2154850

Published online: 06 Jan 2023.

ENGINEERING APPLICATIONS OF COMPUTATIONAL FLUID MECHANICS
2023, VOL. 17, NO. 1, 2154850
https://doi.org/10.1080/19942060.2022.2154850

Numerical investigations of pipe flow downstream a flow conditioner with bundle of tubes

Guang Yin [a], Muk Chen Ong [a] and Puyang Zhang [b]

[a]Department of Mechanical and Structural Engineering and Materials Science, University of Stavanger, Stavanger, Norway; [b]State Key Laboratory of Hydraulic Engineering Simulation and Safety, Tianjin University, Tianjin, People's Republic of China

ABSTRACT

Flow conditioners are widely utilized in pipeline systems to improve the precision of flow rate measurement in the pipeline systems of the offshore and subsea oil and gas industry. There is a lack of knowledge about the influences of the conditioners on the flow inside a bend pipe due to the measurement inaccuracy caused by geometries complexity. In this study, numerical simulations are carried out solving the three-dimensional Reynolds-averaged Navier-Stokes (RANS) equations with the $\kappa-\omega$ SST model to investigate the large-scale flow characteristics inside a double bend pipe and the performance of a conditioner with a bundle of 19 tubes. The obtained axial velocity inside a double bend pipe flow with no flow conditioner are compared with those of the previously published numerical simulations results and experimental data as the validation study. Helical flow structures are found behind the double bend and effectively removed by the flow conditioner. The performance of the flow conditioner is evaluated based on the axial flow velocity profiles, the swirl intensities and the deviation from the flow inside a straight pipe. The effects of Reynolds numbers and the lengths of the tube bundle on the flow downstream the flow conditioner are discussed.

ARTICLE HISTORY
Received 1 August 2022
Accepted 29 November 2022

KEYWORDS
Flow conditioners; 3D RANS; pipe flow; the k-ω SST turbulence model

Nomenclature

D	Pipe diameter
r	Radial position
R	Pipe radius
Rc	radius of the bend
Re	Reynolds number
ν_T	Turbulent eddy viscosity
ν	Kinematic viscosity
u_i	Reynolds-averaged velocities
I	Turbulence intensity
l	Turbulent length scale
U_m	Bulk velocity
x	Pipe axis location
Ld	Pipe length downstream the tube bundle
Lu	Pipe length before the bend
Lt	Length of the tube bundle
k	Turbulent kinetic energy
ω	Specific turbulence dissipation rate
ε	Turbulent dissipation

Abbreviations

SST shear stress transport

1. Introduction

In the pipeline systems for oil and gas in subsea and offshore technology, due to the space limitations, the pipelines are not always straight. The transport of fluids through bend sections, which are used as fittings in pipeline systems, is commonly observed. The redirection of the flow after a bend section will generate a centrifugal force along the cross section acting on the fluid particles. The centrifugal force is proportional to U^2/R (the value U represents the characteristic axial velocity inside the pipe flow and R represents the curvature radius of the bend section). Therefore, the centrifugal force is larger around the centerline of the pipe than that near the pipe walls due to the higher flow velocity along the pipe centerline than that near the pipe walls, where the flow velocity is almost zero because of the nonslip condition at the wall. As a result, the force sweeps the flow near the pipe axis towards the outer wall of the bend. When the flow reaches the outer wall of the bend, it will move back along the wall in the azimuthal direction towards the inner side of the bend. Then, a secondary flow in a pair of counter-rotating motions within the cross section will be induced, which is called Dean vortices (Dean, 1927). The Dean

CONTACT Puyang Zhang zpy@tju.edu.cn

vortices continue to exist along the pipe flow after the bend. The properties of this secondary flow created by a single bend have been extensively studied using experiments. For example, Sudo et al. (1998) obtained the mean velocities and also the Reynolds stress inside a 90° bend by the means of laser doppler velocimetry. Kalpakli and Örlü (2013) used particle image velocimetry (PIV) to study the swirling flow behind a 90° bend. The temporal and spatial evolution of the vortices were also investigated by Hellström et al. (2013) using PIV. To gain better knowledge of the flow structure downstream a bend and the spatial variation of the secondary flow, three-dimensional numerical simulations should be employed. However, a long pipe length is usually required for the fully developed pipe flow. In addition, the high Reynolds numbers of the pipe flow in industries also lead to a high computational cost. Therefore, scale-resolving numerical simulations such as Tanaka and Ohshima (2012) using Large Eddy Simulations (LES) and Wang et al. (2018) using Direct Numerical Simulations (DNS) are rare. Other relevant studies employing scale-resolving simulations are performed for low *Re* flow. The vortex breakdown process behind a bend pipe was studied by Ault et al. (2015) at $Re \sim O(10^2)$ using DNS. The vortex dynamic and characteristic flow structures past a T-junction was studied by Chen et al. (2015) using the linear stability analysis at $Re \sim O(10^2)$. The global stability analysis was adopted by Lupi et al. (2020) to explore the flow transition and coherent flow structure caused by the pipe bend at $Re = 2000 \sim 3000$. Han et al. (2022a) performed DNS for the flow mixing process due to a blind-tee inside a subsea pipeline. The effects of the blind-tee lengths, shapes and *Re* with the range of $500 \sim 1500$ were discussed. For high Re at Reynolds-Averaged Navier-Stokes (RANS) simulations using turbulence models were commonly used by Patankar et al. (1975), Sugiyama and Hitomi (2005), Dutta and Nandi (2015) and Dutta et al. (2016, 2022). It was shown by Hilgenstock and Ernst (1996) and Kim et al. (2014) that a satisfactory agreement with the experimental measurements can be achieved by employing RANS models. Han et al. (2022b) used Reynolds stress model to study the secondary flow characteristics through a double-curved pipe in different configurations. The pipe bend induced corrosion in a two-phase pipe flow was quantified by Liu et al. (2022) using the renormalization group (RNG) $k-\varepsilon$ model combined with the volume of fluid (VOF) method.

It was found that due to the bend sections or other installations such as valves and contraction sections, swirling flows will be generated along the pipe and creates distorted pipe flow velocity profiles and pressure losses. These disturbances will influence the accuracy of the flow rate measurement of the pipe systems. A precise measurement of the flow rate using flow meters is important in industrial applications. For example, in subsea pipeline systems, the flow rate monitoring is crucial for the transport safety and efficiency of oil and gas. In petrochemical industries, the flow rate is an important quantity to control the chemical reactions. Flow meters such as orifice plate (Sahin & Ceyhan, 1996; Tunay et al., 2004; Yin et al., 2021) usually have the best performance when subjected to an axisymmetric pipe flow velocity profile with no swirling flow. Therefore, to achieve an accurate measurement of the flow rate in a pipe system, a flow conditioner is usually installed behind any installation which creates disturbances to the pipe flow and before a flow meter. The objective of installing the flow conditioner is to remove the swirling flow, strengthen the skewed pipe flow and accelerate the recovery of a fully developed pipe flow. There are different types of flow conditioners. The most commonly used types are the perforated plate type introduced by Akashi et al. (1978) and Laws (1990) and the tube bundle type as used in Xiong et al. (2003). The perforated plate type conditioner is a plate of finite thickness with an arrangement of the circular holes. The tube bundle type conditioner usually consists of 19 small tubes of finite length arranged in three concentric circles according to the ISO 5167 standard. The performance of the flow conditioners in reducing the swirling flow after bend sections highly depends on the bends geometries, the flow properties and also the geometries of flow conditioners. Therefore, it is important to investigate the influences of these parameters to achieve optimal design of the flow conditioners. Due to the geometrical complexity of the flow conditioners, early studies on their performances mainly relies on experiments. The effects of different positions of the tube bundle with respect to an orifice flow meter were studied by Karnik (1995) to prove the feasibility of decreasing the deviations of the mean pipe flow caused by a single bend. The flow behavior downstream these two types of flow conditioners has been investigated using experiments by Xiong et al. (2003). It was found that the disturbances created by the flow conditioners decay rapidly downstream. The pressure drops due to the perforated plate inside a pipe flow was investigated by Tanner et al. (2019) using CFD simulations. Swirling flows through a Zanker plate, one of the perforated plate type flow conditioners, were studied using CFD simulations with different turbulence models by El Drainy et al. (2009). The performance of the swirl reduction was proved to be correlated with the thickness of the plate. An increasing plate thickness leads to a decreasing tangential velocity and decreasing swirl angle downstream the plate. Most of the previous investigations focused on the perforated plate type conditioners while the performance

of the tube bundle type has not been completely studied due to the uncertainties and the measurement inaccuracy by carrying out experiments introduced by the complex geometries. However, there is a lack of knowledge on the flow detail inside the flow conditioner and the mechanism of the swirl removal by using the flow conditioner. Furthermore, the perforated properties of the flow conditioner, the nonuniformity and distortion of the pipe flow caused by the flow conditioner results in the difficulty for the scale-resolving numerical simulations especially at high *Re*. The size difference between the small tubes and the pipes bring challenge to the meshing for the simulations.

The purpose of the present study is to conduct a comprehensive investigation using CFD simulations to evaluate the performance of a 19-tube bundle flow conditioner behind an out-of-plane double 90° bend. The influences of *Re* (defined as $Re = U_{\mathrm{m}}D/\nu$. U_{m} is the bulk mean velocity of the inlet flow and D is the pipe diameter) ranging from $10^4 \sim 10^5$ and the length of the small tube on the flow fields downstream the flow conditioner are discussed. To save the computational cost at these high *Re*, Reynolds-averaged equations are solved and the main focus is on the large-scale flow characteristics inside the bend pipe and downstream the flow conditioner in the present study. A hybrid mesh is used within the cross section of the conditioner and a refined mesh is used within the small tube. A unified cross-sectional mesh configuration is used along the whole pipe. It should be noted that different from the single bend section, the pipe flow through the out-of-plane double 90° bend section has not been thoroughly studied using CFD simulations. In addition, compared with the previous experimental studies, detailed three-dimensional information of the flow structures and their spatial variations along the pipe behind the double bend can be obtained. The influence of the flow conditioner on the pipe flow can be better quantified, which can provide further guidance and references for the design of the flow conditioner.

In this paper, the numerical model used to carry out the CFD simulations will be introduced in Section 2, including a detailed grid resolution convergence study and a validation study. Section 3 gives the results and relevant discussions. The main conclusions of the investigation are finally provided in Section 4.

2. Numerical setup

2.1. Governing equations and computational overview

The governing equations solved in the present study are the three-dimensional (3D) steady Reynolds-averaged equations (RANS) for the conservations of mass and momentum of incompressible flow, which are given as

$$\frac{\partial u_i}{\partial x_i} = 0 \tag{1}$$

$$u_j\frac{\partial u_i}{\partial x_j} = -\frac{1}{\rho}\frac{\partial p}{\partial x_i} + \frac{\partial}{\partial x_j}\left[(\nu + \nu_T)\left(\frac{\partial u_i}{\partial x_j} + \frac{\partial u_j}{\partial x_i}\right)\right] \tag{2}$$

where u_i and u_j are the Reynolds-averaged flow velocities. The subscripts $i, j = 1, 2, 3$ refer to the three spatial directions (the corresponding velocity components are also denoted as u, v, w). p is the Reynolds-averaged pressure and ρ is the density of the fluid. The parameter ν is the kinematic viscosity of the fluid. The variable ν_T is the turbulent eddy viscosity under the Boussinesq assumption. The two-equation $k-\omega$ SST turbulence model developed by Menter (1994) is adopted to obtain the values of ν_T. The $k-\omega$ SST turbulence model combines the standard $k-\omega$ model developed by Wilcox (1998) used within the boundary layer in the vicinity of the pipe wall and the standard $k-\varepsilon$ model introduced by Jones and Launder (1973) in the free-stream pipe flow around the pipe axis. The turbulent eddy viscosity is calculated as $\nu_T = a_1 k/\max(a_1\omega, SF_2)$. In this equation, S represent the strain rate, $a_1 = 0.31$ and F_2 is calculated as $F_2 = \tanh(\mathrm{arg}_2^2)$ ($\mathrm{arg}_2 = \max(2\sqrt{k}/0.09\omega y, 500\nu/y^2\omega, y$ is the distance to the wall). Detailed description of the turbulence model can be found in Menter et al. (2003). The open-source CFD toolbox OpenFOAM is used to solve Eqs. (1) and (2). The toolbox uses a finite volume method. The steady-state solver simpleFoam, which is based on a semi-implicit method for pressure coupling equations (also known as the SIMPLE algorithm), is used to solve the steady governing equations using iterations. The spatial discretization schemes for the gradient terms in the governing equations are Gauss linear. For the divergence terms, the Gauss linear corrected scheme is used. All these spatial discretization schemes are in the second order. The residuals of all solved quantities after the iterations at each step of the SIMPLE algorithm are kept below 10^{-6} for all simulation cases. It is also worth mentioning that the large-scale secondary flow structures induced by the pipe bend are caused by the centrifugal forces acting on the flow and they can still exist after time-averaging of the flow data according to Kalpakli Vester et al. (2016). Therefore, the spatial distribution and evolution of the steady secondary flow inside the bend pipe can be obtained by solving steady governing equations and the steady simulations were also carried out in many previously published studies such as Thakre and Joshi (2000), Arvanitis et al. (2018), Ayala and Cimbala (2021), Ault et al. (2015), Jurga et al. (2022) and Han et al. (2022b).

Flows inside a bend pipe with and without the 19-tube bundle flow conditioner are simulated to gain an intuitive knowledge on the swirling flow removal. For the one without the flow conditioner, the computational domain as shown in Figure 1(a) consists of a pipe with an axial length of $Lu = 30D$ installed upstream the bend section and another pipe with an axial length of $Ld = 64D$ ($D = 0.1$m) installed downstream the bend section. The axial length of the pipe installed upstream the bend section is set the same as that used in Reghunathan Valsala et al. (2019) and the axial length of the pipe installed downstream the bend section is even larger than that used in Dutta et al. (2016). A 2×90^{o} out-of-plane double bend is used to connect the upstream and downstream pipes. The value of the curvature ratio (defined as Rc/D where Rc is the radius of the center pipe axis in the bend section) is 2. For the one with the flow conditioner as shown in Figure 1(b), the distance between the tube bundle inlet and the outlet of the bend section is $Lb = 2D$, which is the same as that used in the experiments in Xiong et al. (2003). The origin of the global coordinate system is set at the inlet of the conditioner as shown in Figure 1(a). Different lengths of the tube bundle Lt are considered. The wall thickness of the small tubes is set to be $0.02D$ and the outer diameter of the small tubes is set to be $0.18D$. The selection of these parameters of the small tubes is based on the ISO 5167 standard and the sizes of engineering products.

The boundary conditions of the flow quantities for solving the governing equations are prescribed as follows: at the inlet, a fully developed turbulent pipe flow is assumed and the radial profile for the axial velocity is approximated by the 1/7th power law of $U(r)/U_{\max} = (1 - r/R)^{1/7}$, where r is the radius of the pipe and $U_{\max}$ is chosen to achieve a bulk velocity of $U_{\mathrm{m}} = 1$m/s. The value of k and ω at the inlet are given as $k = 1.5(U_{\mathrm{m}}I)^2$ according to Dutta et al. and $\omega = \sqrt{k}/l$ where I represents the turbulence intensity calculated as $I = 0.16(Re)^{-1/8}$ and $l = 0.038D$ is the length scale of the turbulent pipe flow. The normal gradient of the pressure at the inlet of the pipe is prescribed as zero. At the pipe outlet, the normal gradients of the three velocity components and k, ω are set as zero. A reference value of zero is used for the pressure at the pipe outlet. On the wall surfaces of the pipe and the tubes of the conditioner, a nonslip condition is prescribed for the three velocity components. The standard near-wall conditions are applied for the value of k and ω, which is the same as used in Yin et al. (2021). An averaged value of $y^{+} = \Delta y u_{*}/\nu$ (Δy is the distance between the center of the first grid and the pipe wall and u_{*} is the friction at the wall) in the range of $30 \sim 40$ at the pipe wall is maintained for all the simulations since the wall function is used

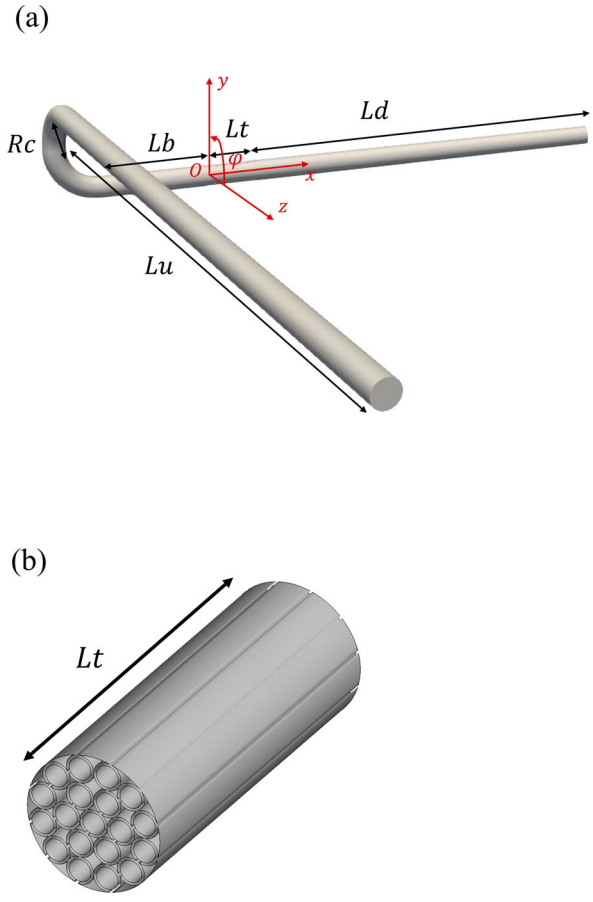

Figure 1. Computational domain (a) the two-90-degree out-of-plane double bend; (b) the tube-bundle flow conditioner.

to resolve the near-wall boundary layer in the present study. It worth mentioning that although it is difficult for the two-equation turbulence models based on the eddy viscosity hypothesis such as the present adopted $k - \omega$ SST model to predict the curvature effects at the bend section. However, the Reynolds stress transport models, which can capture the curvature effects, may lead to a high computational cost and numerical instability issues due to the geometrical complexity of the flow conditioner. In addition, it was shown by Kim et al. (2014) as well as Reghunathan Valsala et al. (2019) that a satisfactory agreement of the resulting velocity profile with the experimental data in the bend can be obtained by using the $k - \omega$ SST model.

2.2. Mesh convergence study and validation study

The grid resolution studies are conducted for the bend pipe with a flow conditioner at $Re = 1 \times 10^5$ to determine the optimal grid resolutions. The curvature ratio is $Rc/D = 1$ and length of the conditioner is $Lt = 2.5D$. These values are set similar to those used in the experiment setups as reported by Xiong et al. (2003).

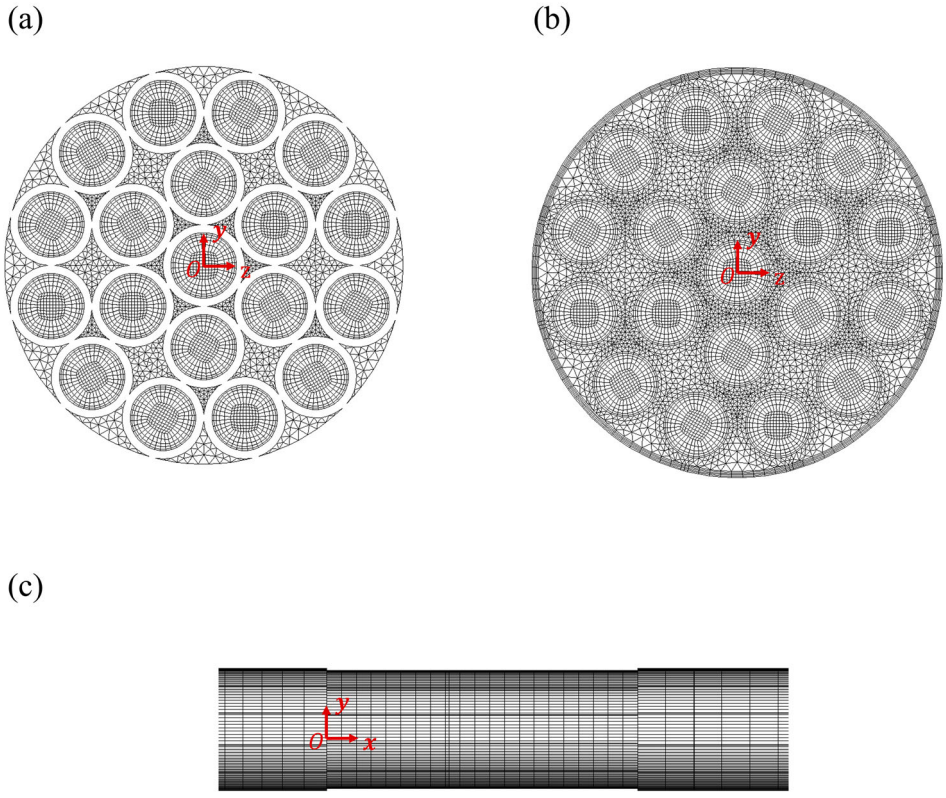

Figure 2. An example of the meshes (a) the cross section of the flow conditioner; (b) the cross section of the pipe; (c) the XY view of the flow conditioner.

To discretize the complex tube bundle region, a hybrid mesh is used within the cross section of the conditioner as shown in Figure 2(a), where a structured mesh is used within the small tube and an unstructured mesh is used between the small tubes. This cross-sectional mesh configuration is also used along the pipe section with an additional refinement close to the pipe wall as shown in Figure 2(b). The cross-sectional grids are extruded along the pipe axis direction to form the three-dimensional grids as shown in Figure 2(c). Using this meshing method, there is no need to set additional transition meshing regions between the main pipe flow part and the flow conditioner part, where the tube diameter is much smaller than that of the pipe. The total grids numbers for each case are M1: 3898746 cells; M2: 5453937 cells; M3: 11419618 cells; M4: 15616958 cells. The axis velocity profiles $u(r)/U_{\max}$ for different meshes at different distances to the conditioner outlet are shown in Figure 3. It can be observed that there is an overall agreement of the velocity profiles between the different meshes. At the distance of $\Delta x/D = 0.5$ close to the outlet of the flow conditioner, there are small differences between each mesh. This may be due to the sensitivity caused by the interaction between the strong jet flows out of the small tubes. However, at further downstream locations, the velocity profiles obtained using different meshes display no significant difference. Therefore, it can be concluded that that the grid resolution of M2 can be regarded as sufficient to balance the mesh convergence and computational cost.

For the validation study, the simulation for the flow inside the double bend pipe without the flow conditioner using the same grid resolutions of M2 is carried out. The obtained radial profiles of the axial velocity at several axial locations along the pipe are selected and compared with the experimentally measured profiles and the CFD simulations results using the $k-\varepsilon$ turbulence model reported by Hilgenstock and Ernst (1996) at $Re = 2.25 \times 10^5$ in Figure 4. The axis velocity profiles at a distance of $x/D = 5$ to the outlet of the bend for four different traverse angles ($\varphi = 0^o, 45^o, 90^o, 135^o$ as shown in Figure 1) are compared in Figure 4. An overall good agreement can be observed. It can be seen that at $\varphi = 0^o$ as shown in Figure 4(a), the high-speed region close to $z = R$ is pushed towards the wall compared with the experimental measurement. Around this region, this difference is also observed for the numerical simulation using the $k-\varepsilon$ turbulence model. There is also an overprediction of the

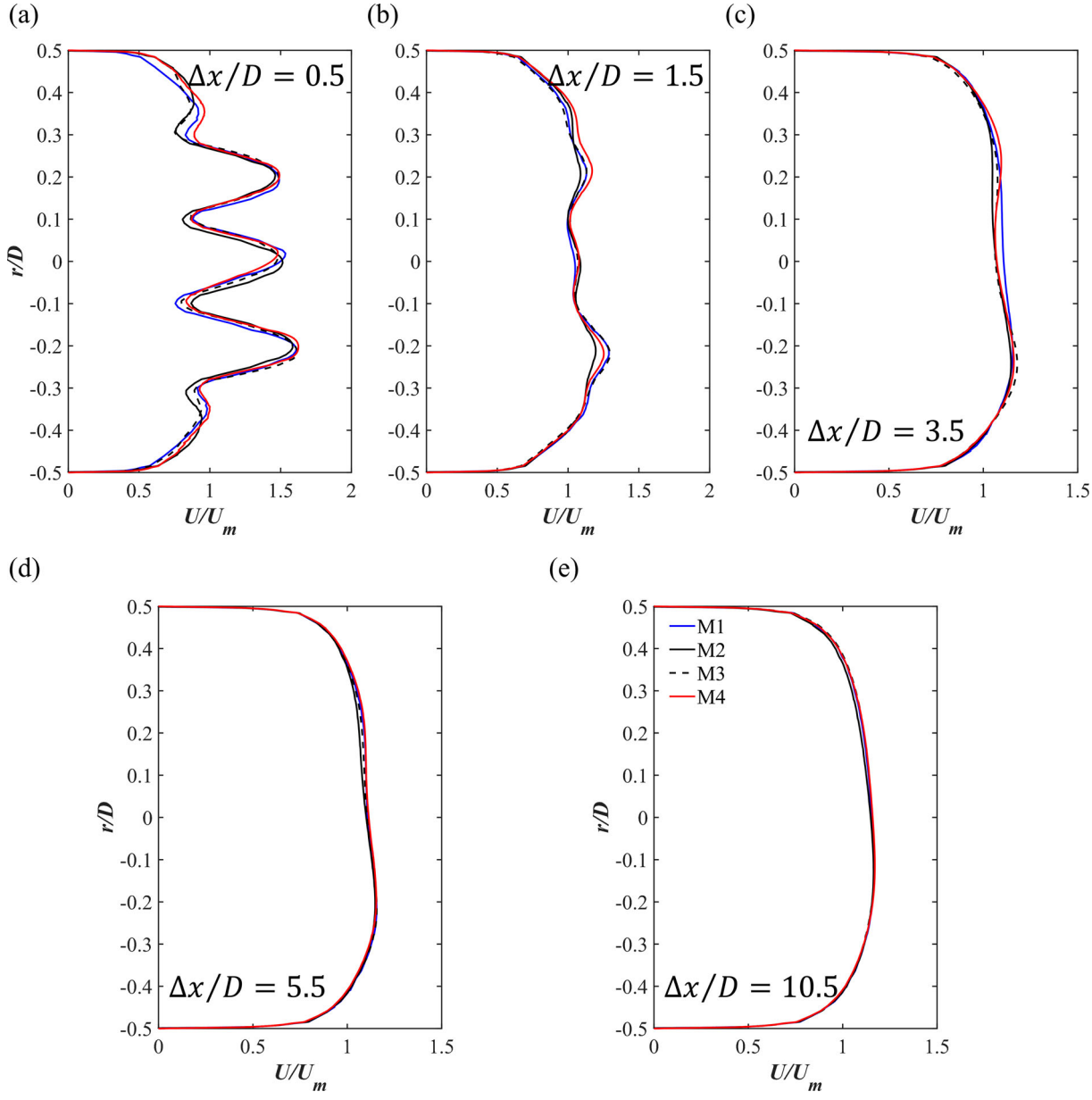

Figure 3. The axis velocity profiles behind the flow conditioner for different meshes.

near-wall velocity around the low-speed region close to $z = -R$ and the wall-normal gradient of the near-wall velocity is larger compared with the experimental data. At $\varphi = 45^{o}$ in Figure 4(b), there is an underestimation of the velocity in the low-speed region close to $z = R$. These differences near the pipe wall may be due to the sensitivity caused by the flow separations in the presence of the bend section. The average relative deviations of the velocity profiles at the two angles of $\varphi = 0^{o}$ and 45^{o} between the experimental data and the present numerical simulations are 4.87% and 4.4%, respectively. At $\varphi = 90^{o}$ shown in Figure 4(c) and 135^{o} shown in Figure 4(d), the velocity profiles obtain by the present numerical model are close to the experimental measurements. Especially, the two peaks of the axis velocity close to $z = \pm R$ and the concave region close to the center axis at $\varphi = 90^{o}$ are well predicted by the present numerical simulations. The average relative deviations of the predicted velocity profiles from the experimental data at $\varphi = 90^{o}$ and 135^{o} are 4.6% and 2.2%

3. Results and discussions

3.1. Flow fields without the flow conditioner

Firstly, the flows downstream the double bend without the flow conditioner are presented to display the

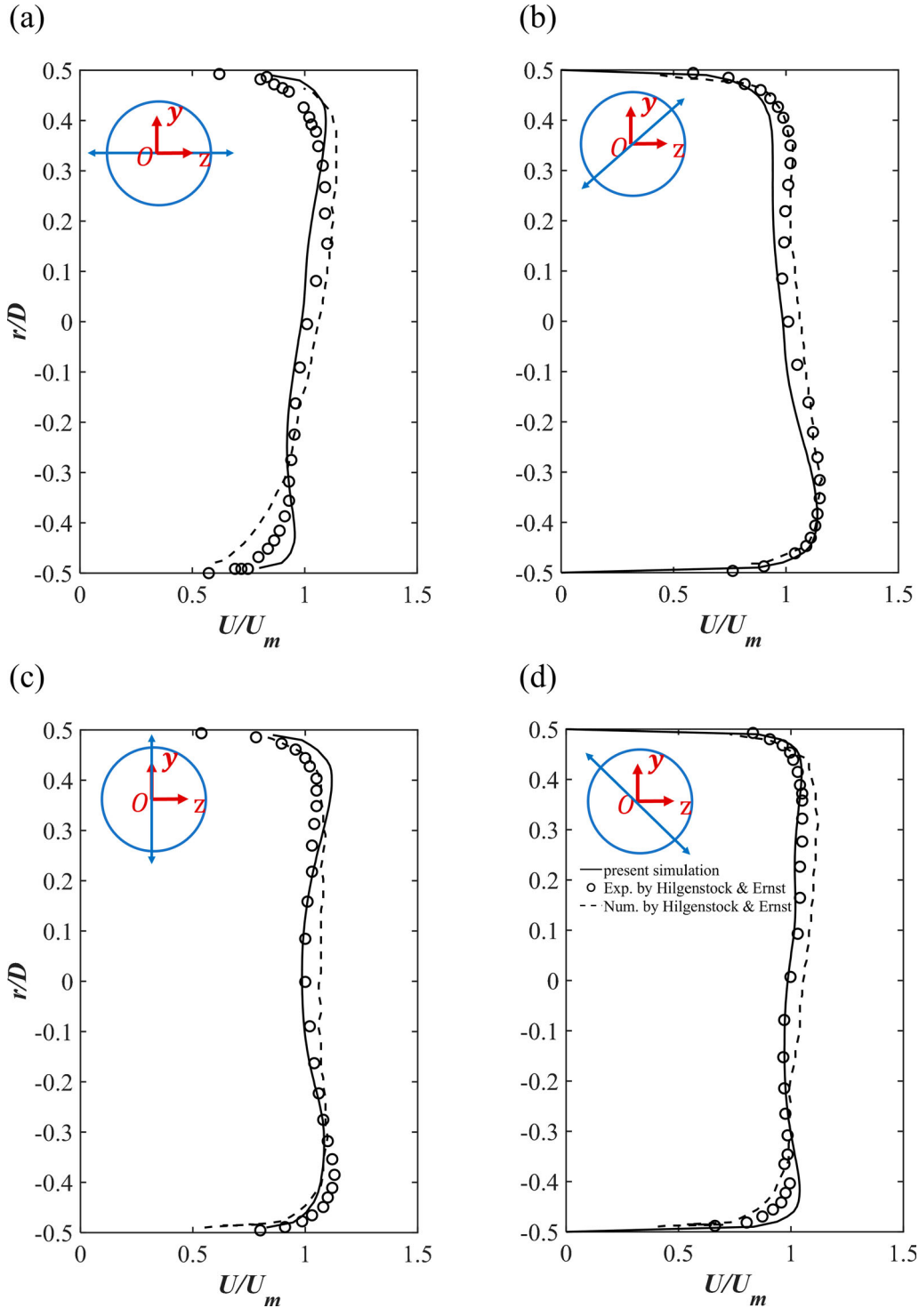

Figure 4. The present predicted axis velocity profiles at a distance of $x/D = 5$ to the outlet of the bend for four different traverse angles (denoted by the arrow) compared with the experimental data and numerical results reported in Hilgenstock and Ernst (1996).

influence of the double bend on the pipe flow. The vortical structures inside the pipe are identified using λ_2 criterion, which is calculated as the second largest eigenvalue of the symmetric tensor $S_{ij}S_{ij} + \Omega_{ij}\Omega_{ij}$. In this equation, S_{ij} and Ω_{ij} represent the symmetric and anti-symmetric parts of the gradient tensor of the flow velocity. Figure 5 shows the 3D iso-surfaces of λ_2 for the perturbation velocity defined as $\mathbf{u}' = \mathbf{u} - U_{sm}\mathbf{n}$, where $\mathbf{n}$ is the unit vector normal to the cross section and $U_{sm}(r)$ is fully developed turbulent pipe flow approximated by the 1/7th power. There are strong vortical structures filling the pipe bend part. In the further downstream region, different

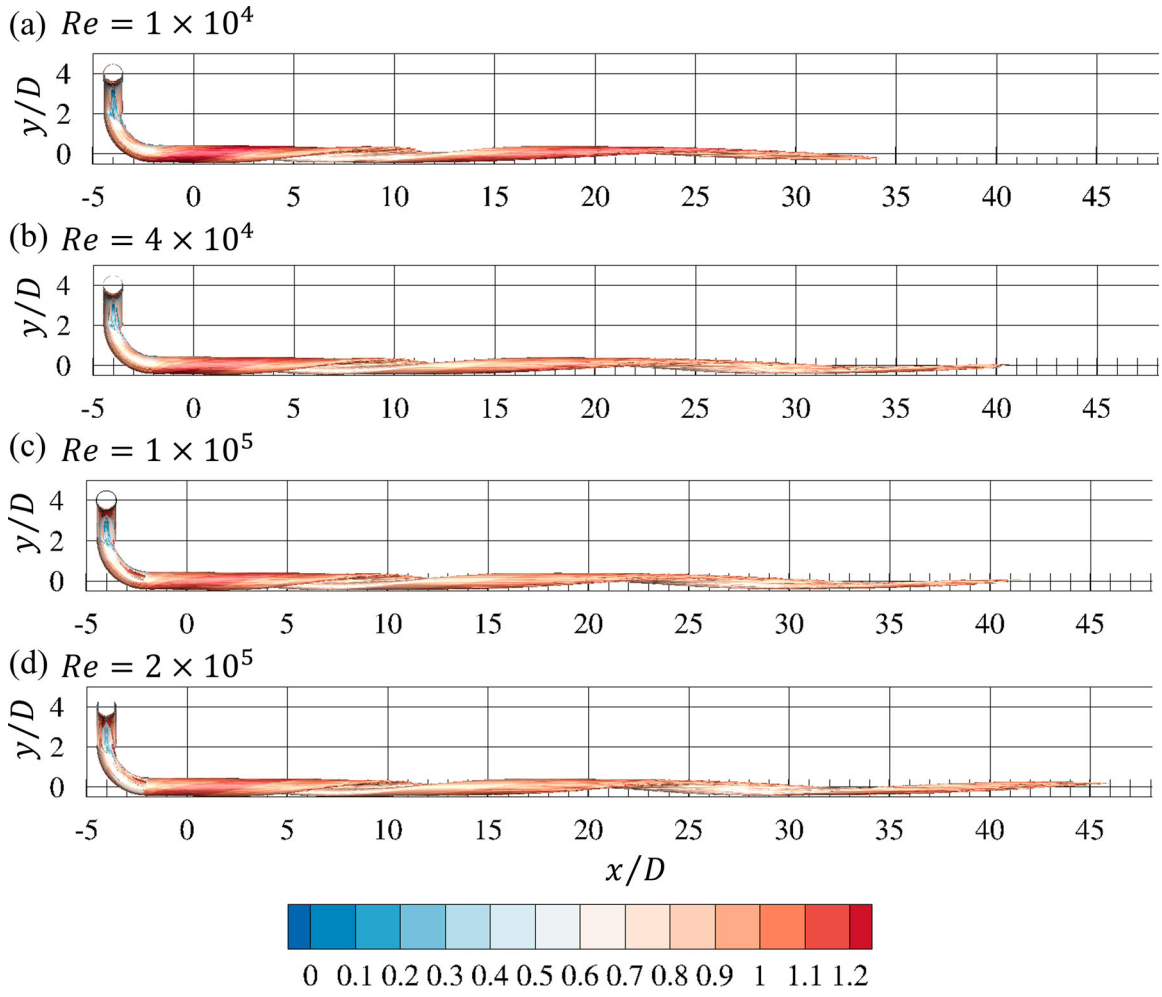

Figure 5. The iso-surfaces of $\lambda_2 = -8$ coloured by the velocity amplitude for the perturbation velocity.

from the two straight tube-like structures indicating the counter rotation vortices observed downstream a single pipe bend or a T-junction (Ault et al., 2015), a long helical structure is presented and can exist up to $x/D \sim 40$. In addition, with the increasing *Re*, the decay length of the vortices becomes longer. The streamlines for different *Re* at different streamwise locations of $x/D = -2, 1$ and 10 after the double bend are shown in Figure 6. The streamlines are coloured by the in-plane tangential velocity given as $||\mathbf{u} - \mathbf{u} \cdot \mathbf{n}||/U_{\mathrm{m}}$($U_{\mathrm{m}}$ is the bulk velocity). It can be seen that close to the bend pipe at $x/D = -2$, there are multiple recirculation motions and strong tangential motions between these motions. Two small secondary motions (denoted as 'S') are shown in Figure 6(a,b) close to the corner of the cross section. With the increasing *Re*, the secondary motions become weaker while in the downstream regions, the tangential motions become stronger, which can be observed at $x/D = 1$. At $Re = 2.0 \times 10^5$, the secondary motions almost disappear and the tangential motions energy seem to be more distributed on the cross section compared with that of the low *Re*.

3.2. Influences of the flow conditioner on the flow fields

The influences of the flow conditioner on the flow field downstream are then examined in the comparison of axis velocity profiles at $\varphi = 90^{\mathrm{o}}$. Several streamwise locations of $x/D = 3, 5, 10, 15, 20$ and 30 between the bend pipe with and without the flow conditioner at $Re = 1.0 \times 10^5$ as shown in Figure 7. At $x/D = 3$ close to the flow conditioner, there are strong jet flows indicated by three sharp peaks. Compared with that without the conditioner which are skewed and asymmetric, the small tubes tend to recover the symmetry of the radial profiles of the flow velocity. From $x/D = 5 \sim 20$, there is a changing asymmetry in the velocity profiles for the case without the conditioner which is indicated by the changing location

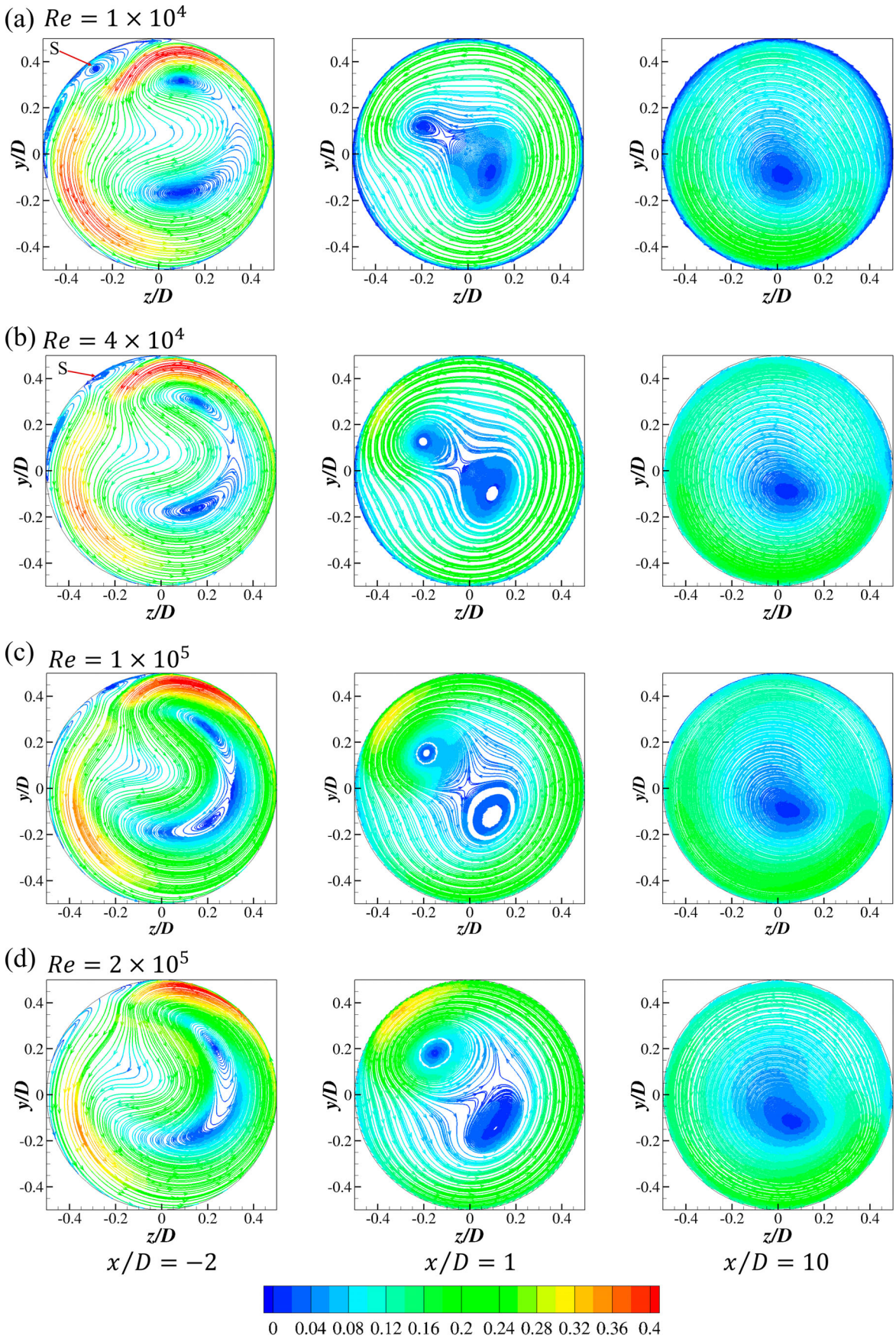

Figure 6. Streamlines for different *Re* at three selected streamwise locations.

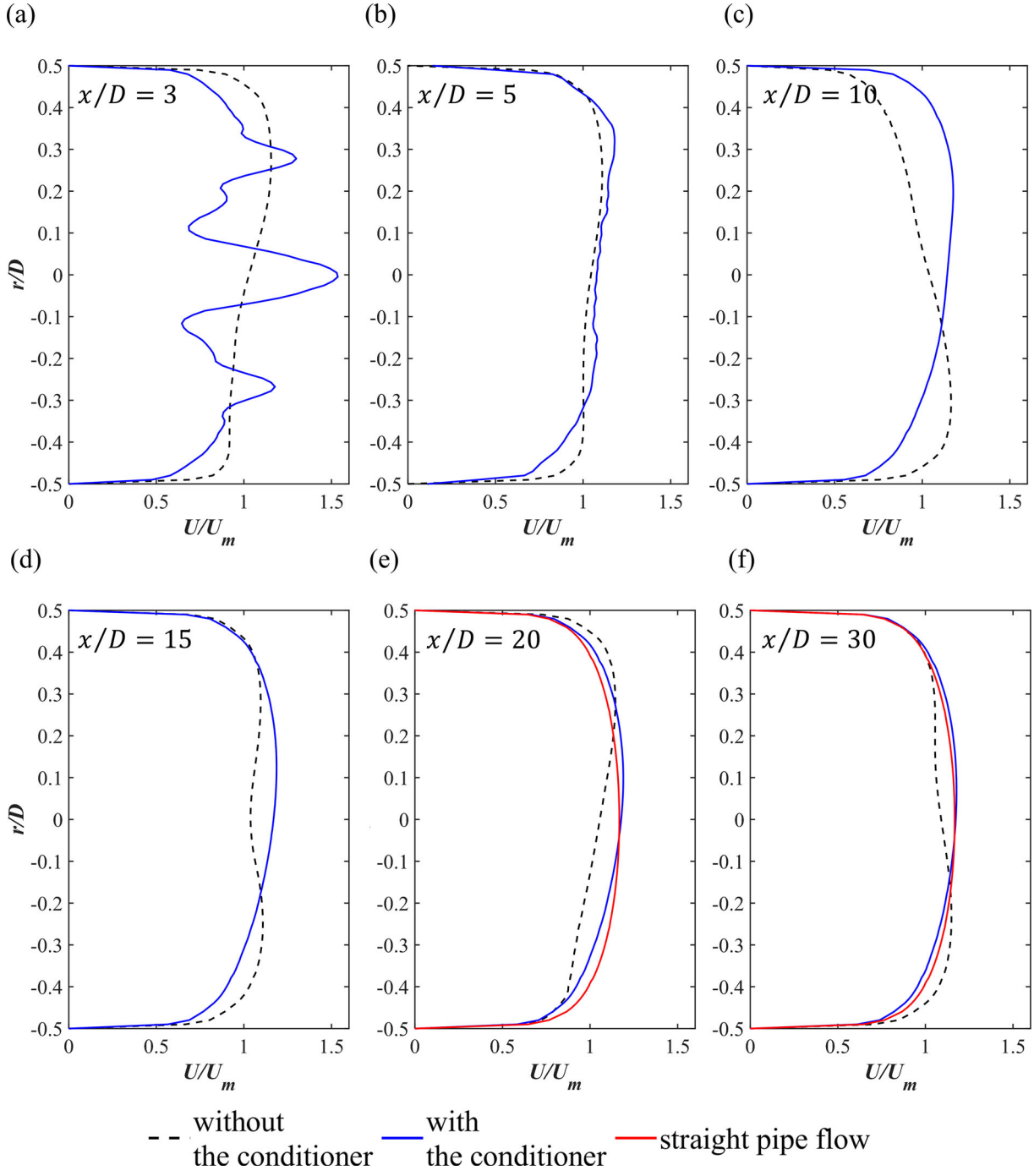

Figure 7. The comparison of axis velocity profiles between the case with and without flow conditioner at the same streamwise locations.

of the high-speed region. This is due to the helical flow behind the double bend as will be shown later. For the case with the flow conditioner, the strong jet flows quickly decay at $x/D = 5$ shown in Figure 7(b). Figure 7(c,d) show that the velocity profile becomes bulged around the center pipe axis. The slight asymmetry of velocity profile becomes weaken in the further downstream region. It becomes close to the velocity profile of the straight pipe flow after $x/D = 20$ as shown in Figure 7(e,f), which indicates that an accurate measurement of the flow rate can be obtained after this location. The comparison of the tangential velocity profile for the two cases at $x/D = 3, 20$ and 30 is shown in Figure 8. It can be seen that there remains a strong cross-sectional motion at $x/D = 20$ while the conditioner can effectively remove this motion and the tangential velocity almost disappear.

For the two cases, Figuer 9. shows the comparison of the axis velocity contours at the locations of $x/D = -2$ before the flow conditioner; $x/D = 1$ within the flow

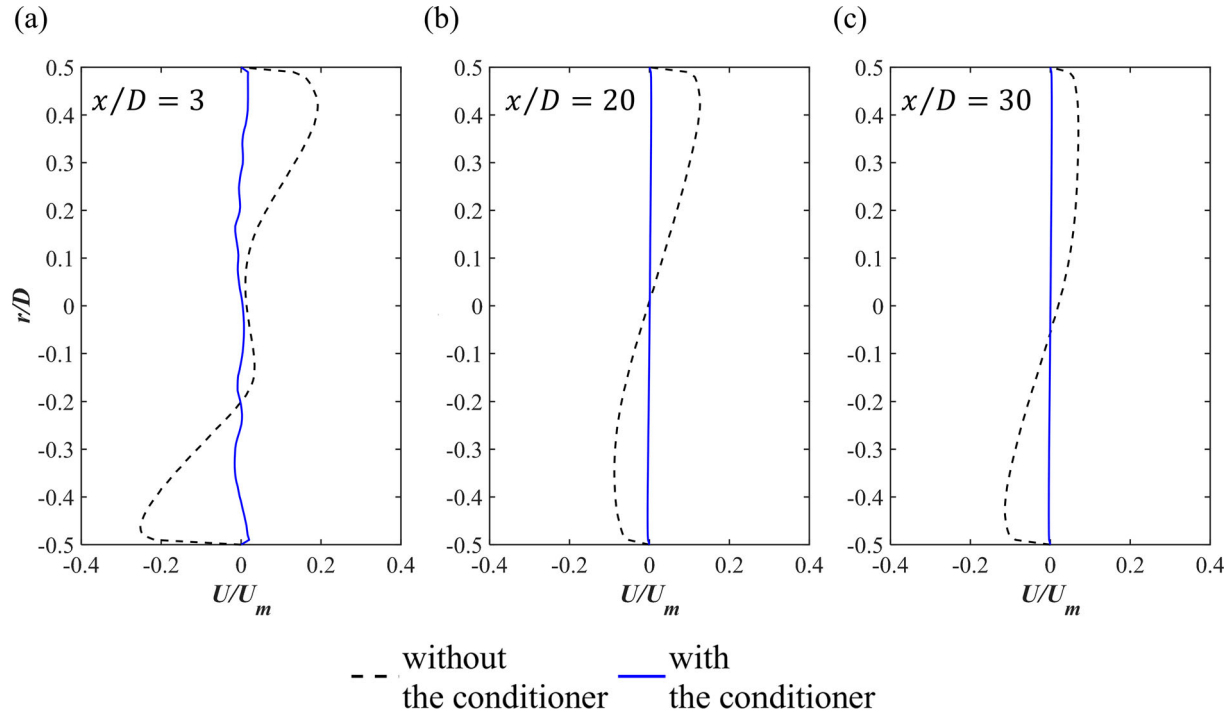

Figure 8. The comparison of the tangential velocity profiles between the case with and without flow conditioner at the same streamwise locations.

conditioner; $x/D = 4$ close to the outlet of the flow conditioner and three locations of $x/D = 20, 30$ and 40 in the downstream region. It can be seen that after the double bend, the two cases are similar and the flow is highly deformed with two peaks located close to the pipe wall. A weak separation indicated by a negative axis velocity happens close to the upper wall due to the second bend. For the case with no conditioner, there is only one peak region of the axis velocity further downstream. However, different from that observed after a single bend where the location of the peak value region remains unchanged along the pipe axis as widely reported in Patankar et al. (1975), Sugiyama and Hitomi (2005) and Dutta et al. (2016, 2016), the second bend breaks the symmetry of the contours and the peak value region rotates in the cross section. For the case with the flow conditioner, the flow is highly accelerated within the tubes and between the tubes. Finally, in the further downstream region, the peak value region becomes almost a circle around the center line of the pipe. The cross-sectional streamlines for the two cases at three streamwise locations are shown in Figure 10. There are two vortex cores with counter rotating secondary motions close to the double bend while in the further downstream region, only one vortex core remains, which is different from the flow behind a single bend. For the case with the conditioner, the breaking of the large counter rotating secondary motions into some small pieces by using the small tubes as shown in Figure 10(e). There are still randomly distributed vortex cores after the conditioner. Due to their smaller size compared with the cross-sectional secondary motions, they are quickly dissipated downstream. In the far field downstream, although there is still cross-sectional rotation, its strength is much weaker than that without conditioner as indicated by the tangential velocity in Figure 10(d).

The comparison of the three-dimensional streamlines colored by the velocity magnitudes for the two cases is shown in Figure 11. For the case with no conditioner, the distorted flow velocity profiles are due to the skewed streamlines after the bend. Within the second bend section, the flow in the outer side is skewed towards the inner side. There seems to be multiple small vortex tubes close to the bend outlet. In the downstream region, the overall pipe flow is highly swirled and helical. However, for the case with the conditioner, the swirled flow after the bend is confined within the small tubes and forced to accelerate and becomes streamlined after the tube bundle. The axis vorticity ω_x contours on the cross section at some streamwise locations are also shown in Figure 12. The ω_x contours obtained in the downstream region behind a single bend pipe flow are shown in Figure 12 (b) for comparison. Behind a single bend, the positive and negative ω_x are almost symmetry with almost the same strength due to the counter rotating motions. However, the negative ω_x behind the double bend is largely dominant and because of the helical flow,

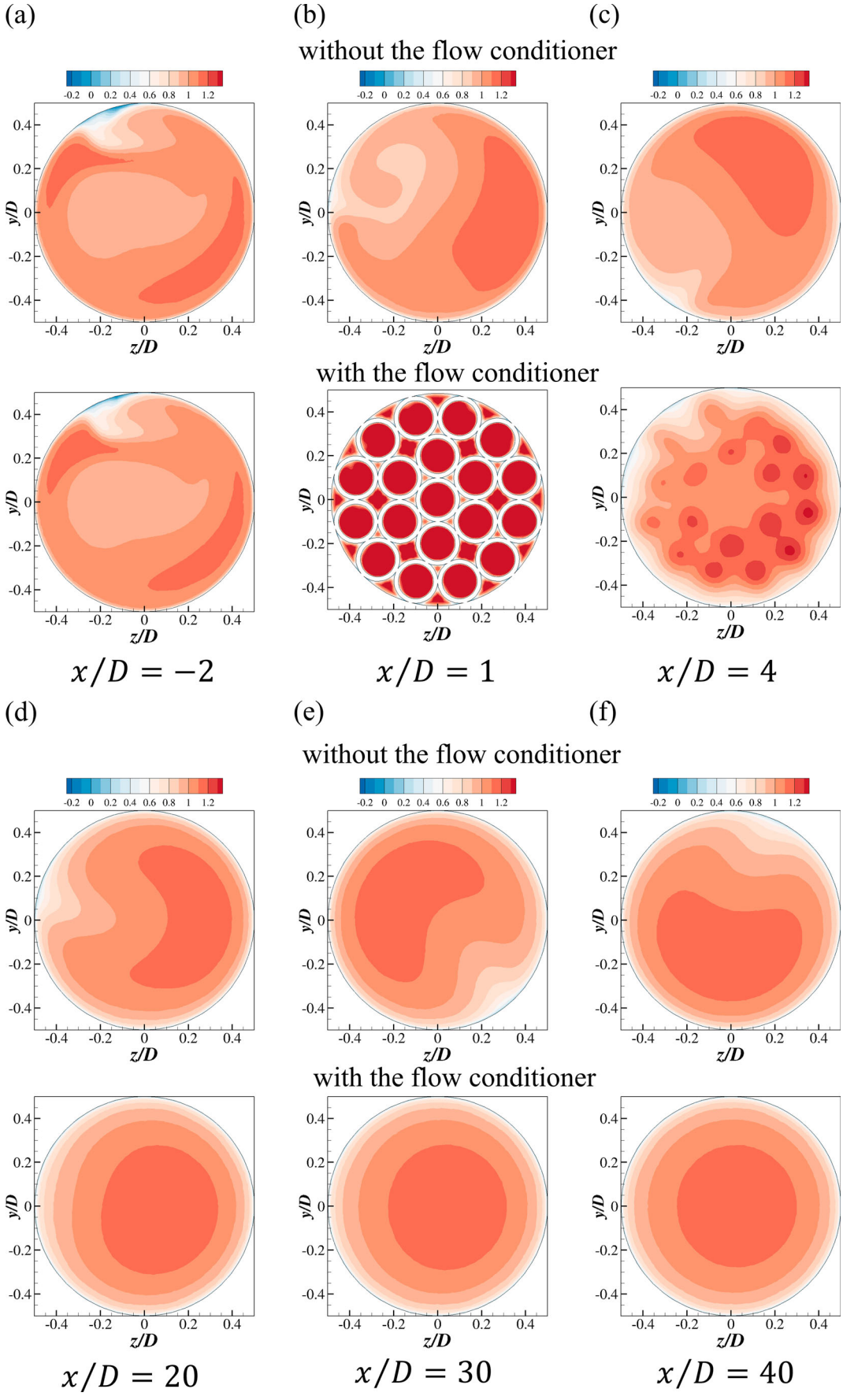

Figure 9. The contours of the axis velocity at different axial locations.

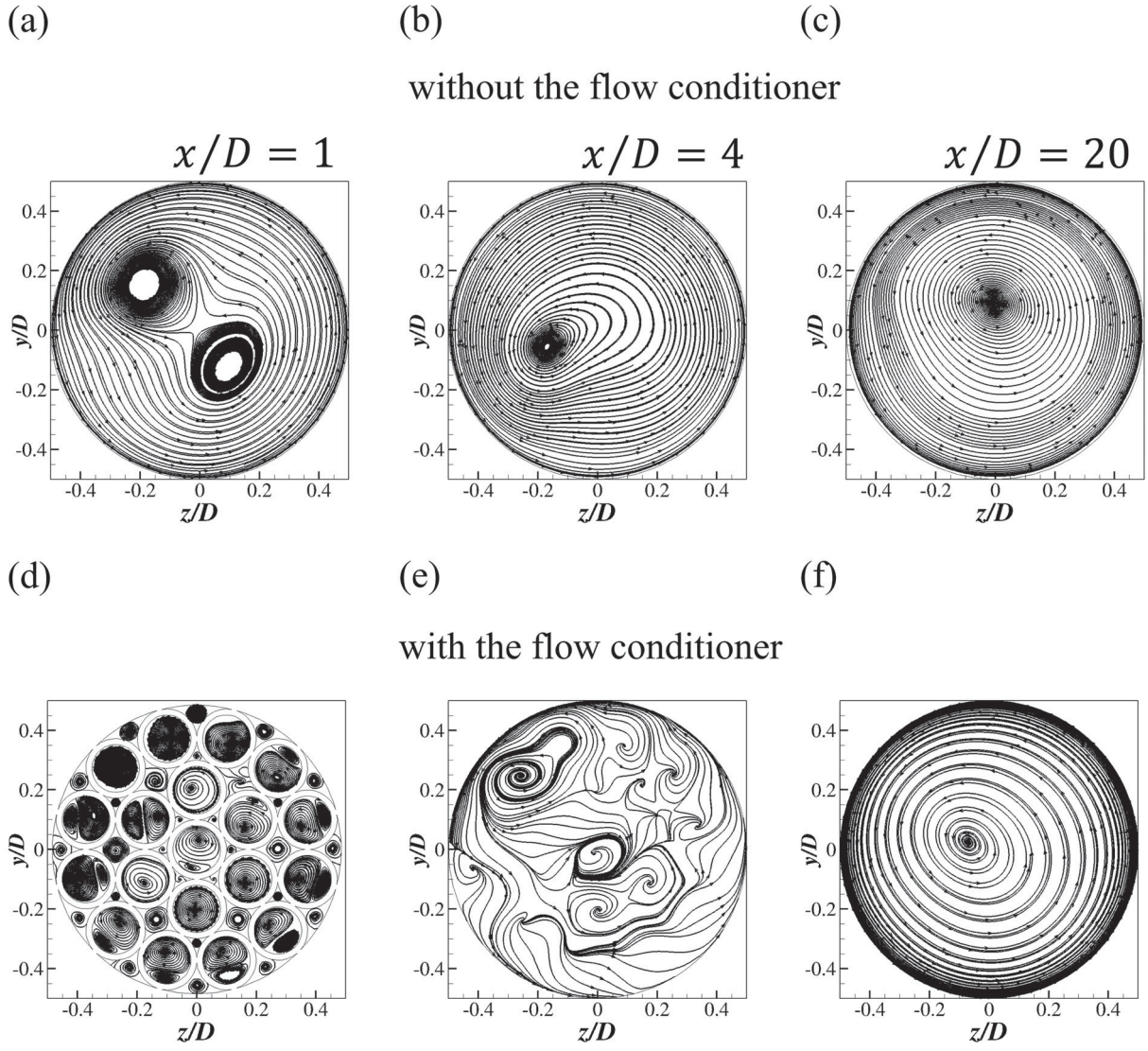

Figure 10. The cross-sectional streamlines at three different axial locations.

the high ω_x region also rotates within the cross-sectional planes along the axis direction. The sign of ω_x is determined by the relative position between the upstream and downstream pipes. With the conditioner, there remains small-scale ω_x with high intensities at $x/D = 1$ and after $x/D = 3$, ω_x almost disappears. Figure 13 shows the comparison of the 3D iso-surfaces of λ_2 at the same level for the perturbation velocity $\mathbf{u}'$ with and without the conditioner. Although there remain some small-scale structures right after the conditioner, a significant removal of the vortical structures in the downstream region is achieved by the conditioner.

To quantitatively evaluate the performance of the flow conditioner on the removal of the swirling flow, the deviation of the axis velocity from that inside a straight pipe as calculated by $D_v = \int |U - U_{sm}| dr / \int |U_{sm}| dr$ (where $U_{sm}(r)$ is the fully developed velocity profile at the same *Re* inside a straight pipe) are measured. Figure 14 shows D_v at different transverse angles along the pipe axis for the two cases with and without the flow conditioner. It can be seen that without the conditioner, there are periodical increase of D_v due to the helical flow caused by the double bend, which are also alternate for the four θs. The spatial periodicity between two peaks may be due to the radius of the bend section. As indicated by Han et al. (2022b), a decreasing bend radius may decrease the spatial periodicity between the two peaks in D_v and as a result, a faster decay of the deviation from the straight pipe flow may be expected due to the energy dissipation of the helical motions. With the conditioner, the values of D_v are significantly reduced. However, since the helical flow structures are not homogenous along the azimuthal direction in the cross section, the reduction of D_v are different for the four transverse directions. The velocity

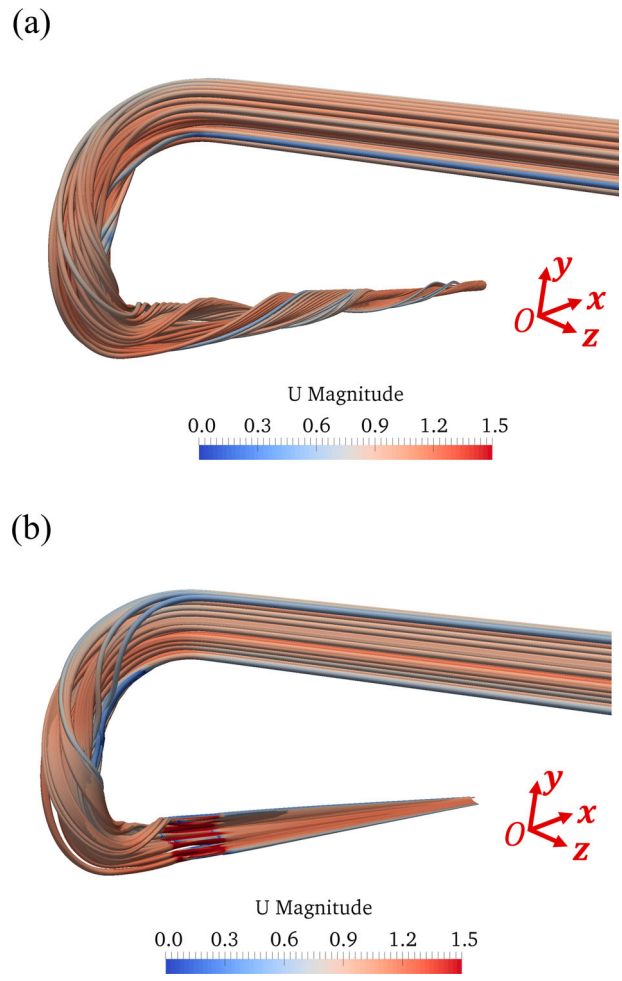

Figure 11. The three-dimensional streamlines coloured by the velocity magnitudes: (a) without the flow conditioner; (b) with the flow conditioner.

profile in the vertical direction is closest to that in a straight pipe while in the horizontal direction there is still deviation from the straight pipe. Therefore, special consideration should be given to the nonuniform reduction of D_v in different radial direction for the double bend in the conditioner design. Due to the removal of the helical flow, the deviation monotonically decays along the axis direction. The values of D_v with the two cases at two different *Re* of $Re = 1 \times 10^4$ and 1×10^5 are further compared in Figure 14(b). It seems that the reduction of the deviation from the straight pipe achieved by the conditioner is independent on *Re*.

3.3. Swirl intensity and the turbulent fluctuation

The swirl intensity is calculated by $I_s = \int [\mathbf{u} - (\mathbf{u} \cdot \mathbf{n})\mathbf{n}]^2 \, dA / (U_m \int dA)$ (where $\mathbf{u}$ is the velocity vector and $\mathbf{n}$ is the unit vector normal to the cross section and the surface integration is conducted within the cross section as dA) as also used in Kim et al. (2014).

The values of I_s for the case without and with the conditioner ($Lt = 2.5D$) at different *Re* of $Re = 1 \times 10^4$, 2×10^4, 4×10^4, 1×10^5 and 2×10^5 along the axis direction are shown in Figure 15. It can be seen that there is an exponential decay in the values of I_s behind the double bend. In addition, with the increasing *Re*, the values of I_s are almost the same close to the bend section while increases further downstream. The increasing I_s may be due to the increasing inertial effects with the increasing *Re*. With the conditioner, there is an abrupt increase in the values of I_s which may be due to the blockage effects created by the flow conditioner. Inside the small tubes, they are significantly reduced compared with those with no conditioner. This is because of the breaking of the large-scale cross-sectional secondary motions into smaller vortices inside the tube and their energy can be more quickly dissipated. In the further downstream region, the values of I_s also undergo an exponential decay and there is also a *Re* effect on the swirl intensity reduction.

The contours of the turbulent kinetic energy k/u_*^2 (u_* is the friction velocity near the pipe wall) for $Lt/D = 2$ at $Re = 1 \times 10^4$ and 1×10^5 close to the outlet of the flow conditioner on the slice at $z = 0$ are shown in Figure 16. It can be seen that due to the shear layer out of the conditioner, a high turbulent kinetic energy is produced. According to Xiong et al. (2003), the generation of turbulence by the conditioner also promote the recovery of the turbulent pipe flow after the bend. The high k/u_*^2 region around the centerline quickly decays compared with that near the pipe wall. With the increasing *Re*, there is an overall increasing intensity of k/u_*^2 behind the conditioner and especially near the pipe wall.

There is another aspect which should be considered for the design and installation of the flow conditioner. Different lengths of $Lt/D = 2, 3, 4, 5$ of the small tubes at $Re = 1 \times 10^5$ is considered in the present study. The values of I_s for different *Lt* are shown in Figure 17. It shows a similar exponential decay trend for these cases. With the increasing *Lt*, there is a constant decrease of the I_s value, which is due to the enhanced acceleration effects and turbulent productions by the longer small tubes.

Furthermore, the profiles of the Reynolds shear stress $\overline{u_x' u_r'}$ at the transverse angle of $\varphi = 0^o$ for $Lt/D = 2$ and 5 at $Re = 1 \times 10^5$ at the streamwise locations of $x/D = 6, 8, 16$ and 20 are shown in Figure 18. It can be seen that close to the outlet of the conditioner, due to the flow development of the pipe flow through the small tubes, a stronger interaction of the jet flow with the pipe flow and a higher turbulence production is generated, which leads to a higher Reynolds shear stress for

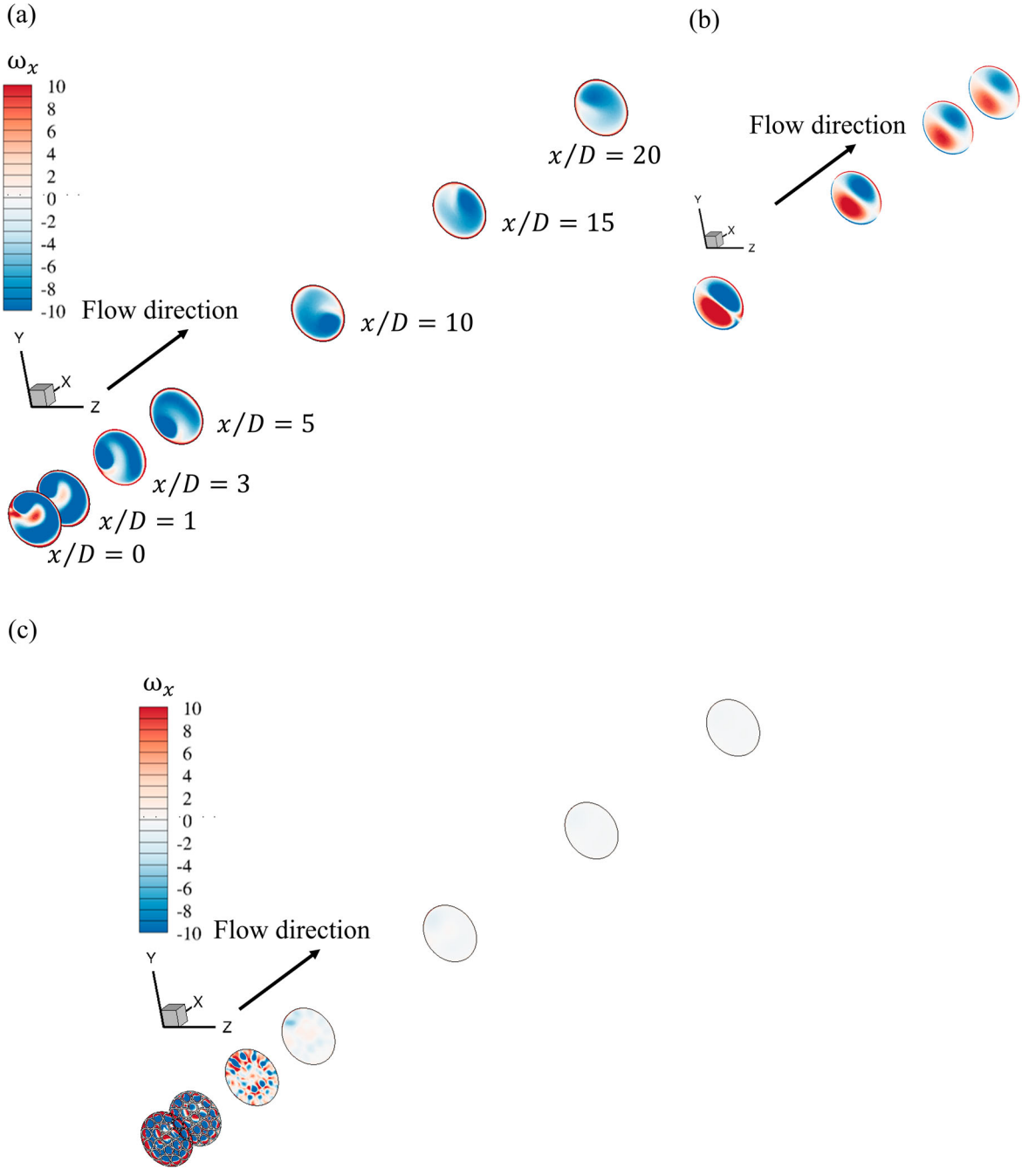

Figure 12. The cross-sectional axis vorticity ω_x contours: (a) with the flow conditioner; (b) behind a single bend section; (c) without the flow conditioner.

$Lt/D = 5$. However, at the same streamwise location of $x/D = 16$ and 20, a similar Reynolds shear stress profile for the two small tube length indicate that the recovery of the turbulent flow field is independent on the length of the conditioner. At $x/D = 16$, the peak values near the pipe wall are already close to those for the straight pipe while there is deformation around the pipe centerline. At $x/D = 20$, although there is a slight deviation, the straight-line behavior in the Reynolds shear stress profile is achieved for the flow conditioner case. This may indicate that increasing the tube length has little effect on enhancing the recovery to the fully developed turbulent pipe flow. For economic consideration, a long flow conditioner may not be a good choice.

4. Conclusion

CFD simulations are conducted to investigate the turbulent flow characteristics through a two-90-degree out-of-plane bend. The performance of a 19-tube-bundle flow

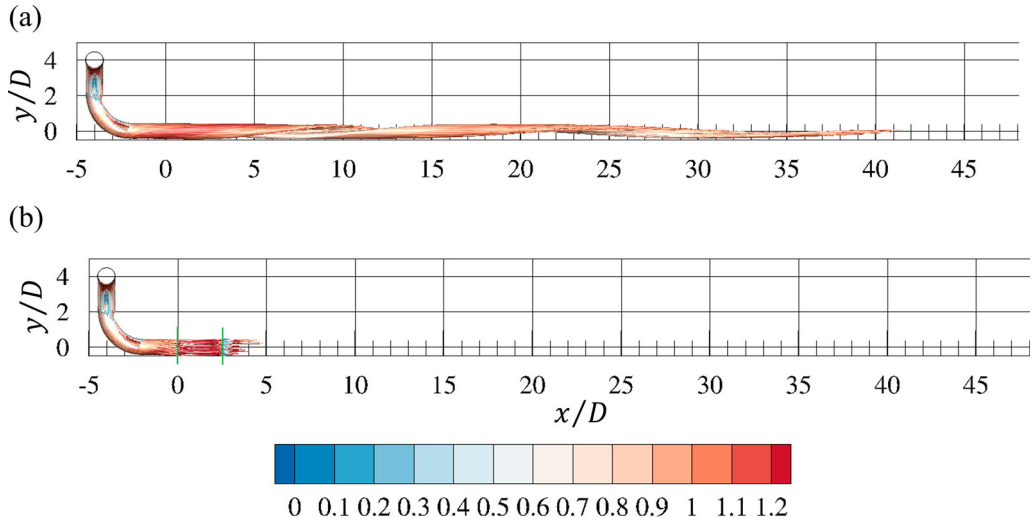

Figure 13. The iso-surfaces of $\lambda_2 = -8$ coloured by the velocity amplitude for the perturbation velocity (a) without the flow conditioner; (b) with the flow conditioner (the green lines indicate the inlet and outlet of the flow conditioner).

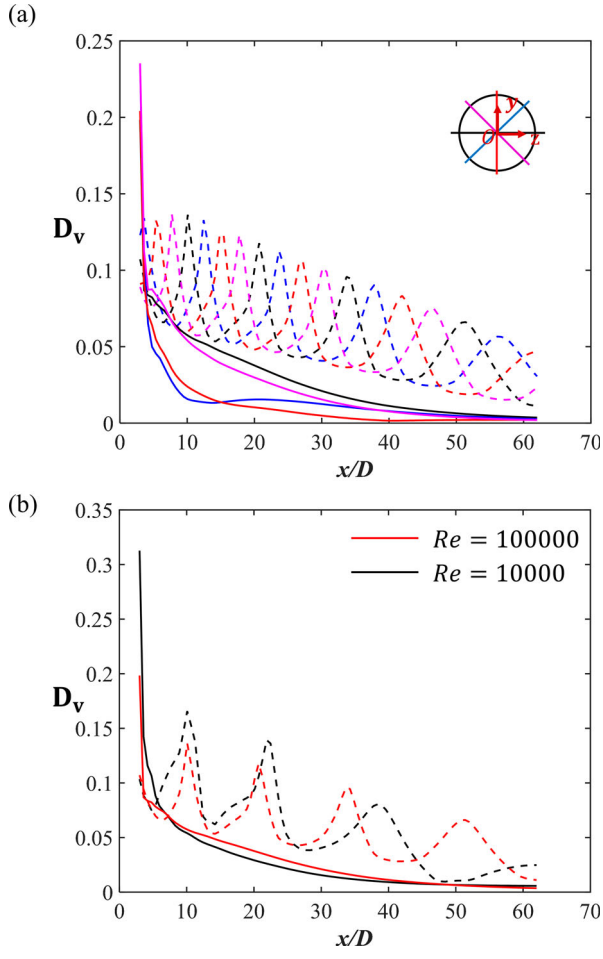

Figure 14. The streamwise variations of the D_v values at different transverse angles (shown in (a)) along the pipe axis with (dashed lines) and without (solid lines) the flow conditioner.

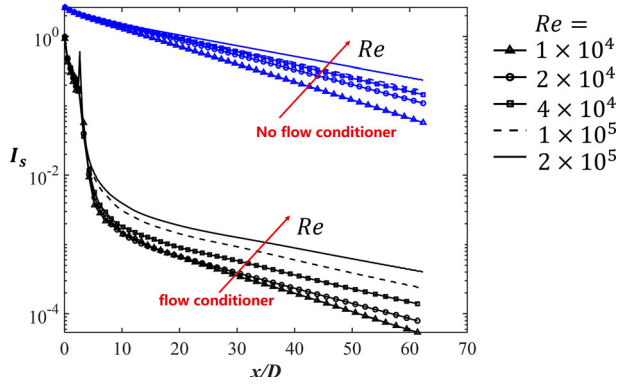

Figure 15. The streamwise variation of the values of I_s with and without the conditioner.

conditioner of reducing the flow swirl and straightening the pipe flow behind the double bend is evaluated. The numerical simulations are performed based on 3D steady RANS equations. The turbulent eddy viscosity is obtained to model the Reynolds stress employing the two-equation $k - \omega$ SST turbulence model. The resulting axis velocity profiles at four transverse directions inside a double bend pipe flow with no conditioner are in a satisfactory agreement with the previously published data by experiments and other numerical simulations, which validates the present numerical model. A detail description of the helical flow structures behind a double pipe bend and their dependence on *Re* are shown. Systematical analysis is conducted based on the overall three-dimensional flow fields, the velocity profiles, the swirling intensity to assess the influence of the flow conditioner. The qualitive and quantitative effects of different *Re* within $O(10^4) \sim O(10^5)$ and the length of

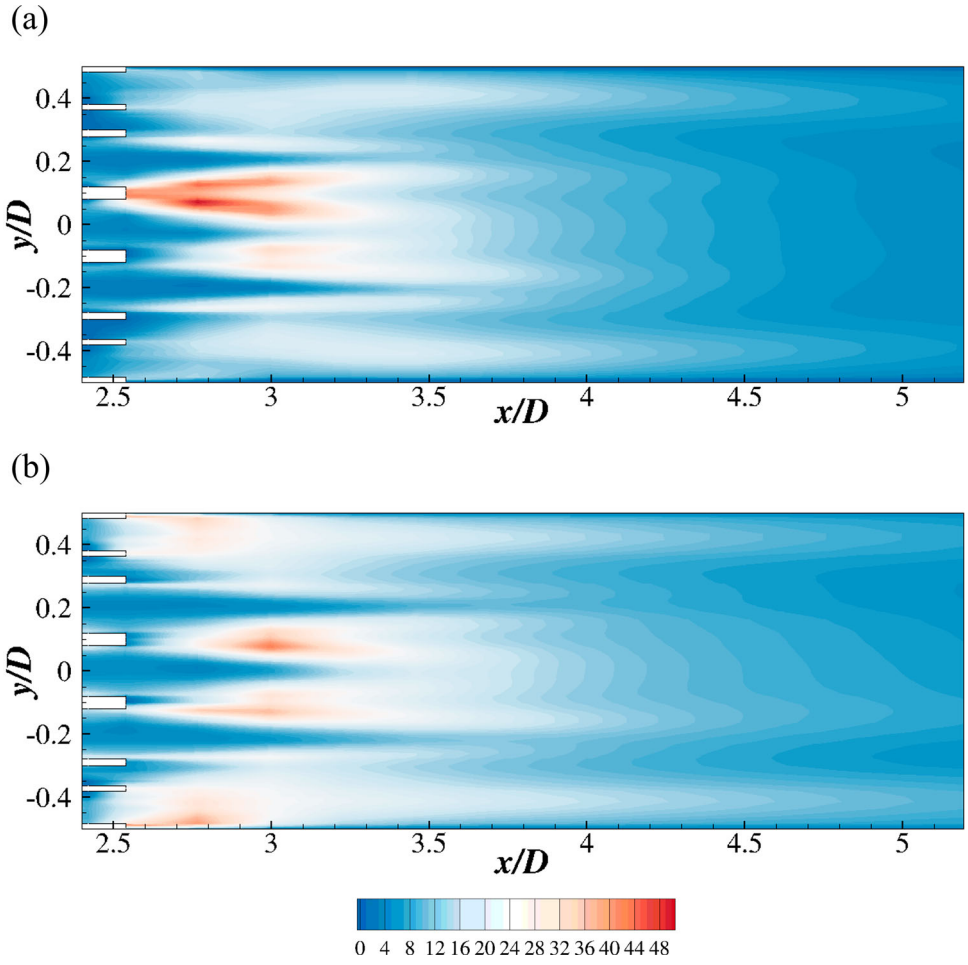

Figure 16. The contours of the turbulent kinetic energy k/u_*^2 at (a) $Re = 1 \times 10^4$ and (b) 1×10^5 close to the outlet of the flow conditioner on the slice at $z = 0$.

the conditioner on the performances are discussed. The main conclusions drawn from this study are outlined as follows:

- The flow behind the double bend is highly distorted and swirled and become helical along the axis direction, which causes different locations of high-speed flow regions and rotating high axis vorticity regions. By using the tube-bundle flow conditioner, the helical flow is removed and straightened to become a fully developed pipe flow. Although there are strong jet flows right after the conditioner due to the flow acceleration of the small tubes, the flow becomes close to the straight pipe flow at around $20D$ behind the conditioner. The tangential velocity is also removed.
- The swirl intensity behind the double bend exponentially decreases along the axis direction and increases with the increasing *Re*. The swirl intensity can be further significantly decreased by the flow conditioner and there is still *Re* effect on the swirl reduction.

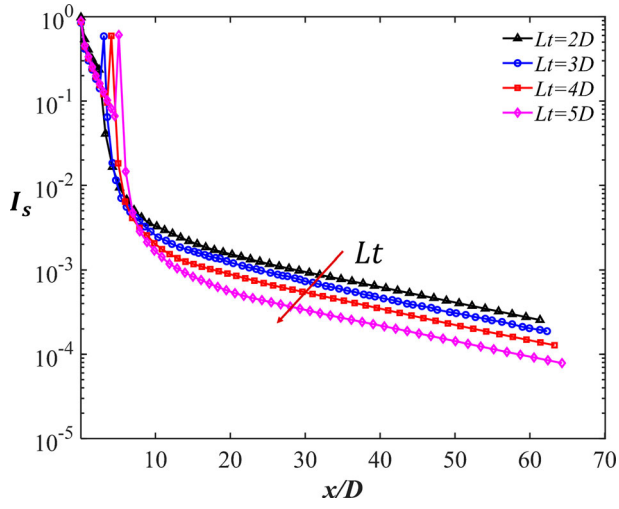

Figure 17. The streamwise variation of the values of I_s for different Lt/D at $Re = 1 \times 10^5$.

- The performance of the conditioner to reduce the swirl intensity slightly increases with the length of the small tubes. Similar Reynolds shear stress profiles

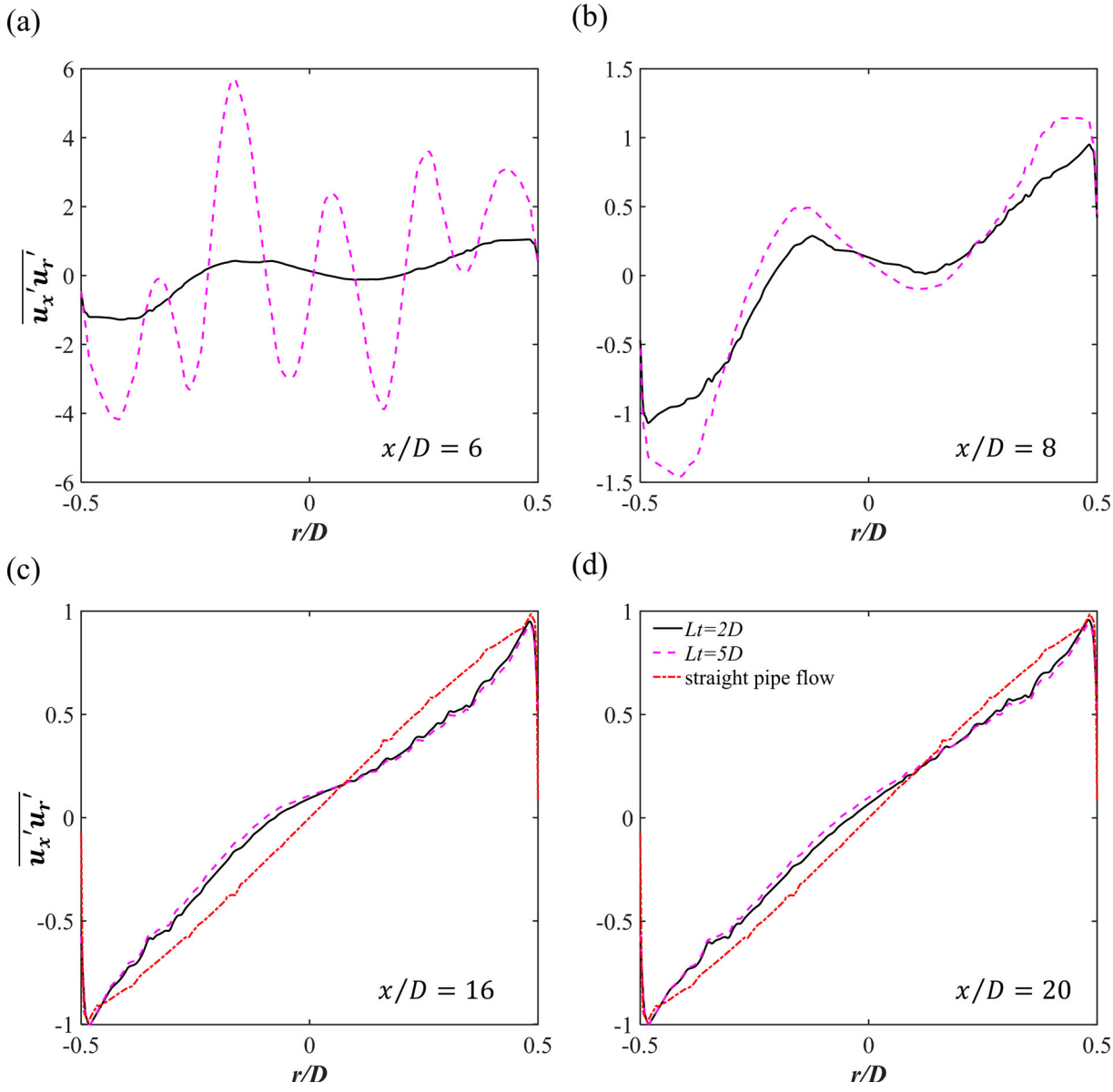

Figure 18. The profile of the Reynolds shear stress $\overline{u_x'u_r'}$ at $\varphi = 0^o$ for $Lt/D = 2$ and 5 at $Re = 1 \times 10^5$ at different streamwise locations.

are obtained downstream the conditioner for different small tube lengths.

The findings through CFD simulations can provide guidance for quantifying and evaluating the performance of the flow conditioners, which is useful for their design and optimization. The present study only considers the 19-tube bundle flow conditioner and the influence of its length on the flow fields in the bend pipe. The performance of other types of flow conditioner for the internal flow inside different pipe configuration such as T-junction, blind-tee or other bending shapes can also be evaluated using the present numerical tool, which can be carried out in the future study. In addition, the unsteadiness of the turbulence properties will be obtained by performing scale-resolving simulations such as Large Eddy Simulations.

Acknowledgement

This study was supported by State Key Laboratory of Hydraulic Engineering Simulation and Safety (Tianjing University) (Project No: HESS-2126) and also with computational resources provided by the Norwegian Metacenter for Computational Science (NOTUR), under Project No: NN9372 K.

Disclosure statement

No potential conflict of interest was reported by the author(s).

Funding

This work was supported by State Key Laboratory of Hydraulic Engineering Simulation and Safety (Tianjing University): [Grant Number HESS-2126]; UNINETT Sigma2—the National Infrastructure for High Performance Computing and Data Storage in Norway [Grant Number NN9372K].

ORCID

Guang Yin http://orcid.org/0000-0001-8448-7183
Muk Chen Ong http://orcid.org/0000-0001-5288-5857
Puyang Zhang http://orcid.org/0000-0003-2344-7262

References

Akashi, K., Watanabe, H., & Koga, K. (1978). Flow rate measurement in pipe line with many bends. *Mitsubishi Heavy Ind*, *15*(2), 87–96.

Arvanitis, K. D., Bouris, D., & Papanicolaou, E. (2018). Laminar flow and heat transfer in U-bends: The effect of secondary flows in ducts with partial and full curvature. *International Journal of Thermal Sciences*, *130*, 70–93. https://doi.org/10.1016/j.ijthermalsci.2018.03.027

Ault, J. T., Chen, K. K., & Stone, H. A. (2015). Downstream decay of fully developed Dean flow. *Journal of Fluid Mechanics*, *777*, 219–244. https://doi.org/10.1017/jfm.2015.353

Ayala, M., & Cimbala, J. M. (2021). Numerical approach for prediction of turbulent flow resistance coefficient of 90° pipe bends. *Proceedings of the Institution of Mechanical Engineers, Part E: Journal of Process Mechanical Engineering*, *235*(2), 351–360. https://doi.org/10.1177/0954408920964008

Chen, K. K., Rowley, C. W., & Stone, H. A. (2015). Vortex dynamics in a pipe T-junction: Recirculation and sensitivity. *Physics of Fluids*, *27*(3), 034107. https://doi.org/10.1063/1.4916343

Dean, W. R. (1927). XVI. Note on the motion of fluid in a curved pipe. *The London, Edinburgh, and Dublin Philosophical Magazine and Journal of Science*, *4*(20), 208–223.

Dutta, P., Chattopadhyay, H., & Nandi, N. (2022). Numerical studies on turbulent flow field in a 90 deg pipe bend. *Journal of Fluids Engineering*, *144*(6), 061104. https://doi.org/10.1115/1.4053547

Dutta, P., & Nandi, N. (2015). Effect of reynolds number and curvature ratio on single phase turbulent flow in pipe bends. *Mechanics and Mechanical Engineering*, *19*(1), 5–16.

Dutta, P., Saha, S. K., Nandi, N., & Pal, N. (2016). Numerical study on flow separation in 90° pipe bend under high Reynolds number by k-ϵ modelling. *Engineering Science and Technology, an International Journal*, *19*(2), 904–910. https://doi.org/10.1016/j.jestch.2015.12.005

El Drainy, Y. A., Saqr, K. M., Aly, H. S., N. Mohd, & Jaafar, M. (2009). CFD analysis of incompressible turbulent swirling flow through zanker plate. *Engineering Applications of Computational Fluid Mechanics*, *3*(4), 562–572. https://doi.org/10.1080/19942060.2009.11015291

Han, F., Liu, Y., Lan, Q., Li, W., & Wang, Z. (2022b). CFD investigation on secondary flow characteristics in double-curved subsea pipelines with different spatial structures. *Journal of Marine Science and Engineering*, *10*(9), 1264. https://doi.org/10.3390/jmse10091264

Han, F., Liu, Y., Ong, M. C., Yin, G., Li, W., & Wang, Z. (2022a). CFD investigation of blind-tee effects on flow mixing mechanism in subsea pipelines. *Engineering Applications of Computational Fluid Mechanics*, *16*(1), 1395–1419. https://doi.org/10.1080/19942060.2022.2093275

Hellström, L. H., Zlatinov, M. B., Cao, G., & Smits, A. J. (2013). Turbulent pipe flow downstream of a bend. *Journal of Fluid Mechanics*, *735*. https://doi.org/10.1017/jfm.2013.534

Hilgenstock, A., & Ernst, R. (1996). Analysis of installation effects by means of computational fluid dynamics – CFD vs experiments? *Flow Measurement and Instrumentation*, *7*(3-4), 161–171. https://doi.org/10.1016/S0955-5986(97)88066-1

Jones, W. P., & Launder, B. (1973). The calculation of low-Reynolds-number phenomena with a two-equation model of turbulence. *International Journal of Heat and Mass Transfer*, *16*(6), 1119–1130. https://doi.org/10.1016/0017-9310(73)90125-7

Jurga, A. P., Janocha, M. J., Yin, G., & Ong, M. C. (2022). Numerical simulations of turbulent flow through a 90-Deg pipe bend. *Journal of Offshore Mechanics and Arctic Engineering*, *144*(6), 061801. https://doi.org/10.1115/1.4054960

Kalpakli, A., & Örlü, R. (2013). Turbulent pipe flow downstream a 90 pipe bend with and without superimposed swirl. *International Journal of Heat and Fluid Flow*, *41*, 103–111. https://doi.org/10.1016/j.ijheatfluidflow.2013.01.003

Kalpakli Vester, A., Örlü, R., & Alfredsson, P. H. (2016). Turbulent flows in curved pipes: Recent advances in experiments and simulations. *Applied Mechanics Reviews*, *68*(5). https://doi.org/10.1115/1.4034135

Karnik, U.. (1995, March 20–22). A compact orifice meter/flow conditioner package. In *Third International Symposium on Fluid Flow Measurement*, San Antonio, TX, U.S.A.

Kim, J., Yadav, M., & Kim, S. (2014). Characteristics of secondary flow induced by 90-degree elbow in turbulent pipe flow. *Engineering Applications of Computational Fluid Mechanics*, *8*(2), 229–239. https://doi.org/10.1080/19942060.2014.11015509

Laws, E. M. (1990). Flow conditioning – a new development. *Flow Measurement and Instrumentation*, *1*(3), 165–170. https://doi.org/10.1016/0955-5986(90)90006-S

Liu, Z., Shao, W. Q., Sun, Y., & Sun, B. H. (2022). Scaling law of the one-direction flow characteristics of symmetric Tesla valve. *Engineering Applications of Computational Fluid Mechanics*, *16*(1), 441–452. https://doi.org/10.1080/19942060.2021.2023648

Lupi, V., Canton, J., & Schlatter, P. (2020). Global stability analysis of a 90°-bend pipe flow. *International Journal of Heat and Fluid Flow*, *86*, 108742. https://doi.org/10.1016/j.ijheatfluidflow.2020.108742

Menter, F. R. (1994). Two-equation eddy-viscosity turbulence models for engineering applications. *AIAA Journal*, *32*(8), 1598–1605. https://doi.org/10.2514/3.12149

Menter, F. R., Kuntz, M., & Langtry, R. (2003). Ten years of industrial experience with the SST turbulence model. *Turbulence, Heat and Mass Transfer*, *4*(1), 625–632.

Patankar, S. V., Pratap, V. S., & Spalding, D. B. (1975). Prediction of turbulent flow in curved pipes. *Journal of Fluid Mechanics*, *67*(3), 583–595. https://doi.org/10.1017/S0022112075000481

Reghunathan Valsala, R., Son, S. W., Suryan, A., & Kim, H. D. (2019). Study on reduction in pressure losses in pipe bends

using guide vanes. *Journal of Visualization*, *22*(4), 795–807. https://doi.org/10.1007/s12650-019-00561-w

Sahin, BEŞİR, & Ceyhan, HÜSEYİN. (1996). Numerical and experimental analysis of laminar flow through square-edged orifice with variable thickness. *Transactions of the Institute of Measurement and Control*, *18*(4), 166–174. https://doi.org/10.1177/014233129601800401

Sudo, K., Sumida, M., & Hibara, H. (1998). Experimental investigation on turbulent flow in a circular-sectioned 90-degree bend. *Experiments in Fluids*, *25*(1), 42–49. https://doi.org/10.1007/s003480050206

Sugiyama, H., & Hitomi, D. (2005). Numerical analysis of developing turbulent flow in a 180 bend tube by an algebraic Reynolds stress model. *International Journal for Numerical Methods in Fluids*, *47*(12), 1431–1449. https://doi.org/10.1002/fld.818

Tanaka, M., & Ohshima, H. (2012). Numerical investigation on large scale eddy structure in unsteady pipe elbow flow at high Reynolds number conditions with large eddy simulation approach. *Journal of Power and Energy Systems*, *6*(2), 210–228. https://doi.org/10.1299/jpes.6.210

Tanner, P., Gorman, J., & Sparrow, E. (2019). Flow–pressure drop characteristics of perforated plates. *International Journal of Numerical Methods for Heat & Fluid Flow*, *29*(11), 4310–4333. https://doi.org/10.1108/HFF-01-2019-0065

Thakre, S. S., & Joshi, J. B. (2000). CFD modeling of heat transfer in turbulent pipe flows. *AIChE Journal*, *46*(9), 1798–1812. https://doi.org/10.1002/aic.690460909

Tunay, T., Sahin, B., & Akilli, H. (2004). Investigation of laminar and turbulent flow through an orifice plate inserted in a pipe. *Transactions of the Canadian Society for Mechanical Engineering*, *28*(2B), 403–414. https://doi.org/10.1139/tcsme-2004-0029

Wang, Z., Örlü, R., Schlatter, P., & Chung, Y. M. (2018). Direct numerical simulation of a turbulent 90 bend pipe flow. *International Journal of Heat and Fluid Flow*, *73*, 199–208. https://doi.org/10.1016/j.ijheatfluidflow.2018.08.003

Wilcox, D. C. (1998). *Turbulence modeling for CFD* (Vol. 2, pp. 103–217). DCW industries.

Xiong, W., Kalkühler, K., & Merzkirch, W. (2003). Velocity and turbulence measurements downstream of flow conditioners. *Flow Measurement and Instrumentation*, *14*(6), 249–260. https://doi.org/10.1016/S0955-5986(03)00031-1

Yin, G., Nitter, B., & Ong, M. C. (2021). Numerical simulations of turbulent flow through an orifice plate in a pipe. *Journal of Offshore Mechanics and Arctic Engineering*, *143*(4). https://doi.org/10.1115/1.4049250